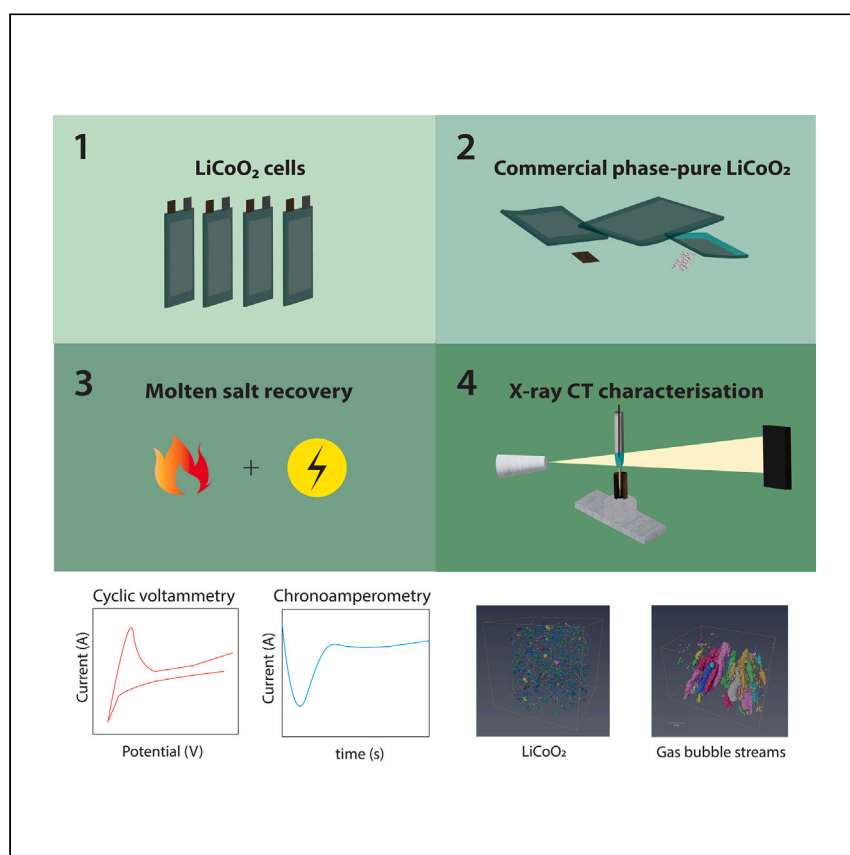**Article**

Electrochemical recovery of lithium-ion battery materials from molten salts by microstructural characterization using X-ray imaging

Mirza et al. report a comprehensive study into the electrochemical recovery of cobalt metal from $LiCoO_2$ using X-ray computed tomography. X-ray computed tomography offers the ability to understand the role of process conditions and cell configurations to optimize a pyro-electrochemical reprocessing technology that can play a key role in sustainable battery recycling.

Mateen Mirza, Wenjia Du, Lara Rasha, Steven Wilcock, Arfon H. Jones, Paul R. Shearing, Dan J.L. Brett

p.shearing@ucl.ac.uk (P.R.S.)
d.brett@ucl.ac.uk (D.J.L.B.)

Highlights

In-depth study of a key battery material, $LiCoO_2$, using LiCl-KCl molten salt

Design of a miniaturized cell for the electrochemical recovery of Co from $LiCoO_2$

Characterization of recovered Co metal morphologies using X-ray computed tomography

Cell Reports
Physical Science

Article

Electrochemical recovery of lithium-ion battery materials from molten salts by microstructural characterization using X-ray imaging

Mateen Mirza,[1,4] Wenjia Du,[1,2,4] Lara Rasha,[1,2] Steven Wilcock,[3] Arfon H. Jones,[3] Paul R. Shearing,[1,2,*] and Dan J.L. Brett[1,2,5,*]

SUMMARY

Recycling spent lithium-ion batteries (LiBs) guarantees the conservation of important metal resources by reducing demands on raw supply and offsetting the energy and environmental costs associated with its manufacture. Employing a molten salt as a solvent for extraction affords a much greener and simpler route to metal recovery by electrochemical means. The current mechanistic understanding of the electrochemical recovery of metals in molten salts needs to be improved for the process to be optimized. X-ray computed tomography offers a non-destructive approach for 3D microstructure visualization and subsequent quantification. Here, we study the electrochemical deposition of recovered cobalt metal from lithium cobalt oxide, $LiCoO_2$ in LiCl-KCl eutectic (LKE). This diagnostic approach has been applied to $LiCoO_2$-LKE samples before and after electrolysis at $450°C$, yielding key insights into the morphological evolution of product formation.

INTRODUCTION

With climate change targets at the epicenter of cleaner technology development efforts, lithium-ion batteries (LiBs) are a cornerstone of the electric vehicle (EV) revolution. More than one-quarter of global carbon dioxide (CO_2) emissions are produced as a by-product of the transportation sector,[1] and the replacement of petrol- and diesel-based vehicles with EVs has led to an unprecedented surge in the LiB market.[2,3] However, managing the industry's dependency on raw material necessitates the need for developing a robust supply chain network. While there has been significant headway made in this regard, selecting practical end-of-life solutions for battery pack waste remains an ever-growing challenge given the projected sale of up to 1 billion EVs in the next 30 years.[4] If we take, for example, an average battery pack at the end of life, which has a weight of approximately 250 kg and a given volume of half a cubic meter, the total resultant pack wastes would lead to the accumulation of 250 million tons and 500 million cubic meters of unprocessed pack waste, posing a serious environmental landfill issue.

Cobalt (Co) metal is currently regarded as a critical material, principally due to its use in LiBs. The supply chain relies on a continuous and stable supply from two major countries, the Democratic Republic of Congo (DRC), which manages 50% of Co reserves and more than 70% of global mine production, and China, whose market share has been steadily increasing since 2002.[5] Of great concern is that most of the mined Co occurs in a mineral deposit form with other elements such as nickel (Ni) or copper (Cu), which means that the market value of Co is susceptible to price

[1]Electrochemical Innovation Lab, Department of Chemical Engineering, University College London, Torrington Place, London WC1E 7JE, UK

[2]The Faraday Institution, Quad One, Harwell Science and Innovation Campus, Didcot OX11 0RA, UK

[3]AWE, Aldermaston RG7 4PR, UK

[4]These authors contributed equally

[5]Lead contact

*Correspondence: p.shearing@ucl.ac.uk (P.R.S.), d.brett@ucl.ac.uk (D.J.L.B.)

https://doi.org/10.1016/j.xcrp.2023.101333

CellPress
OPEN ACCESS

**Cell Reports
Physical Science**
Article

fluctuations in Ni and Cu.[6] With the DRC posing a high risk of political instability, we face an unsettling future. This can be remedied by decentralizing the supply of Co to pave the way for other nations to invest in Co production. While this serves as one option to stabilize the global market supply of Co, the second and more pertinent opportunity is to begin investing in end-of-life waste management processes for spent LiBs.[7]

There is an array of experimental studies that have focused on the recycling strategies for Co and Ni metal from LiB and Ni metal hydride batteries. The hydrometallurgical approach, for example, is an aqueous-based process that enables the extraction of Co metal using a variety of organic and inorganic acids (acetic,[8] sulfuric,[9] and hydrochloric acids[10] in addition to aqua regia) and alkaline solutions (NaOH[11,12]). After acid leaching, a post-treatment purification, solvent extraction, crystallization, or selective precipitation step ensues. On the other hand, the pyrometallurgical process is a mature process, which includes high-temperature roasting and smelting procedures and is a predominant technology in industry with the aim of recovering and purifying commercial-grade metals.[13] Additionally, we appreciate that Li metal is also a critical material and consider it to be an essential element in battery cathode applications. While Li metal is not a point of focus in this paper, there are several methods that may be used in the recovery. One of these methods includes a water-leaching process whereby the obtained spent materials would be ground and then recovered using an air-oxidation water-leaching method at a moderate temperature.[14] Alternatively, vacuum distillation may be employed for the recovery of Li at high temperature, as the metal recovered would possess a much greater melting temperature than the salt.

More recently, the realization that both pyro- and hydrometallurgical processes may be used in tandem has motivated further research and development, and commercially viable technologies have emerged. For example, the Umicore process combines the aforementioned routes by encompassing an incremental heat treatment procedure for the evaporation of electrolyte followed by acid leaching.[15] The key innovation in this process is the management of volatile organic fractions and hazardous gases. Similarly, the Sumitomo-Sony process (also known as the Sony process)[15,16] encompasses an initial calcination step (300°C–700°C) for the removal of both electrolytes and organic binders, leading to the formation of a metallic alloy. The desired metal(s) are then extracted using a suitable leaching process to form CoO rather than Co, which when produced in sufficient quantity can be directly manufactured into LiBs. The commercialization of other technologies has been summarized in further detail by Velázquez-Martínez et al.[2] More recent progress has focused on the use of greener solvents, such as ionic liquids, which are gaining traction in hydrometallurgical processes at room temperature.[17]

Electrochemical recovery processes using molten salt (MS) systems remain a compelling alternative for high-efficiency and green extraction of metals, avoiding the use of hazardous and expensive reducing agents.[18,19] MS processes have the potential to be the next-generation technology to recover metals from secondary resources and reserve metals from primary natural sources. Hydrometallurgical solutions cannot handle low-density metals, and smelting via pyrometallurgical process requires greater heating temperatures (>600°C), while the MS route could extract and refine the light metals (i.e., Al, Li, Mg) and heavy metals (i.e., Co, Ni, Mn) at lower temperatures (<450°C). To date, there has only been limited work on various MS with different precursor designs and electrode materials/sizes as a means to improve extraction efficiencies and reduce carbon emissions.
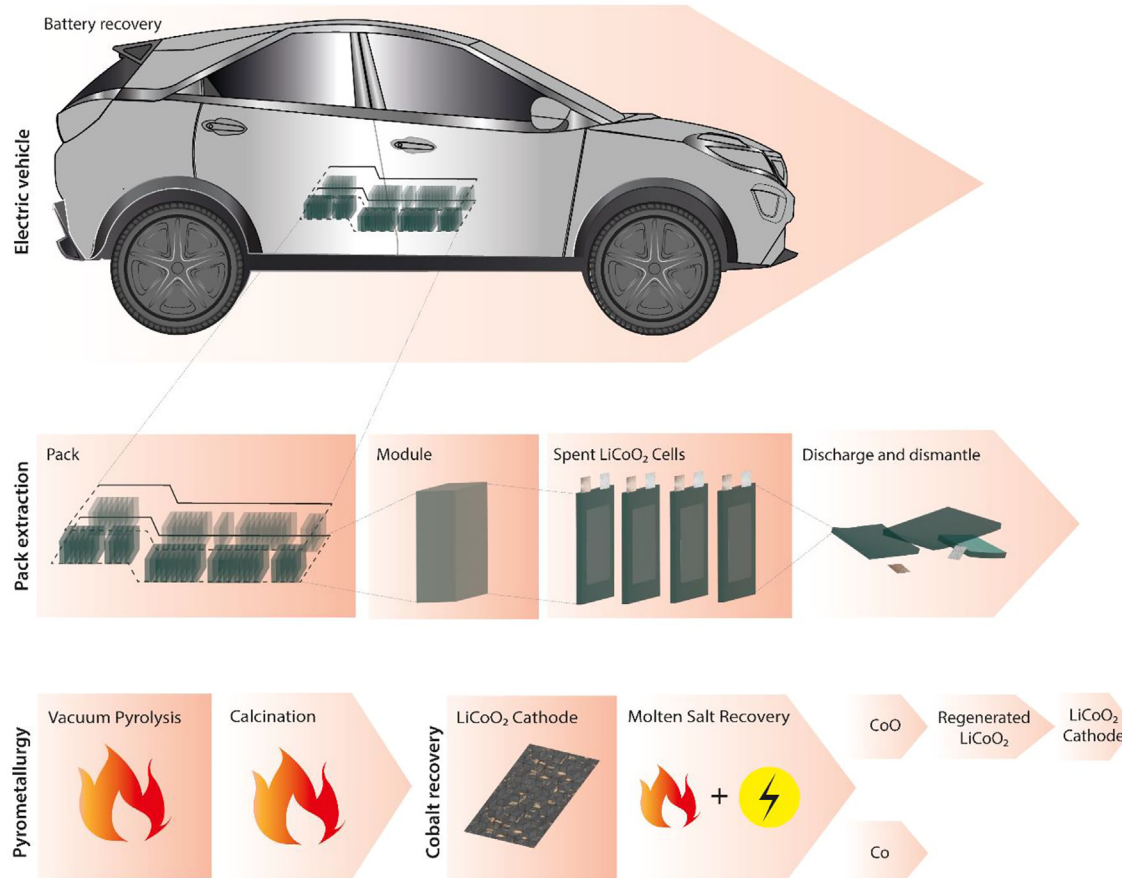
Cell Reports
Physical Science
Article

Figure 1. Flowsheet of cobalt metal recovery from an electric vehicle

The process of Co metal recovery is complex and occurs in several steps, starting with the removal of a pack which houses a battery pack from a vehicle. It is important to note that the pack may be found in different locations, such as the front of the car, near the engine or toward the boot, to improve weight distribution. Such a pack consists of several modules with miscellaneous components including bus bars, electronics, and wiring looms, which are all recoverable components. The $LiCoO_2$ cells are then safely discharged and dismantled within an inert environment. Thereafter, a series of pyrometallurgical steps follow for the removal of organic additives and carbon black. The Co metal or CoO is finally recovered using an MS approach.

MS are a unique class of inorganic, non-aqueous solvents that present favorable electrochemical properties at high temperature. Their large electrochemical windows and high ionic conductivities aid in the electrochemical recovery of metals; the FFC-Cambridge Process was the first technology to pioneer this field by utilizing MS.[20,21] Current progress in the electrochemical extraction of Co metal within MS remains sparse, with only a few studies reporting successful recoveries. One study by Zhang et al.[22] states that with an applied potential of -1.0 V (vs. Ag/Ag$^+$), $LiCoO_2$ (LCO) can be reduced directly to Co metal in Na_2CO_3-K_2CO_3 at 750°C, and another using a fluidized cathode reports that at -2.40 V (vs. Ag/Ag$^+$) in LiCl-KCl eutectic (LKE) at 450°C, Co metal can be recovered.[23] In this process, the metal oxide particles are reduced on the cathode surface and the liberated oxide ions are oxidized at the anode surface. CO and/or CO_2 gas may form as shown in Equations 1 and 2. The flowsheet of a general electrochemical materials recovery process from an EV is shown in Figure 1.

$$C + 2O^{2-} \rightarrow CO_2 + 4e^-, \qquad \text{(Equation 1)}$$

$$C + O^{2-} \rightarrow CO + 2e^-. \qquad \text{(Equation 2)}$$
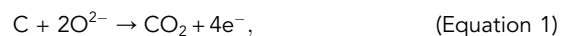
Although there has been progress achieved in the morphological characterization of metal/metal oxide particles following the discovery of the FFC-Cambridge Process and spent nuclear material reprocessing applications using qualitative methods such as scanning electron microscopy (SEM), scanning electron microscopy-energy dispersive spectrometry (SEM-EDS), and transmission electron microscopy (TEM), all of these studies comprise analyses derived from the aforementioned destructive characterization techniques.[24,25] Quantitative studies into the elemental compositions of deposited ferrotitanium alloys in LiCl-Li$_2$O using inductively coupled plasma optical emission spectrometry are also destructive.[26] All of these techniques compromise the structure of the product through exposure to moisture from air, which is worsened by the naturally hygroscopic nature of LKE.

Furthermore, the presence of arbitrary amounts of LKE makes it difficult to quantify the recovery efficiency, and the loss of material following the recovery of metal deposits obscures the holistic understanding of the as-produced material.[27] However, it must be made clear that certain aspects of the MS process, which include electrochemical reactions and resulting compositional changes, may only be clarified with the use of traditional techniques (i.e., SEM, EDS, X-ray diffraction, X-ray photoelectron spectroscopy, and Raman spectroscopy). X-ray computed tomography (CT) is an established technique with multidisciplinary use despite only a few studies focusing on high-temperature applications. These include: exploring the structural integrity of ceramic metal composites,[28] visualizing an MS dealloying procedure[29] and understanding the electrode evolution that occurs in titanium electrorefining.[30] Nevertheless, there is still a void in our understanding of particle morphology in a high-temperature MS system, and the basis of our understanding is still empirical.[31]

Here, we have used X-ray CT to explore the particle evolution following the electrochemical reduction of LCO and to complement existing characterization techniques. This tool provides unprecedented insight into a small-scale MS cell in three dimensions following various applied potentials; to the authors' knowledge, both the experimental design and implementation of this tool are the first of their kind in this application and should help electrochemists in rationalizing and optimizing cells for the complete electrochemical reduction of metal oxide particles while also providing a fundamental understanding of the process to reduce the energy consumption when recycling LiBs. 3D microstructures have been captured to resolve the lithium oxide particles and recovered metal after the MS process.

RESULTS AND DISCUSSION

Electrochemical characterization

Transient electrochemical testing, comprising cyclic voltammetry and chronoamperometry, was performed on a tungsten-fused capillary tube with the diameter of the working electrode measuring 1.5 mm. An in-depth study is presented herein with several cyclic voltammograms (CVs) of the LCO-LKE system performed at scan rates within the region of 30–50 mV s^{-1}. To help orientate the reader, the figures may be referred to by their case number for purposes of clarity, and further details can be found in Table 1. The immersion depth of tungsten metal within LKE was measured to be ca. 1.2 mm for cases 1 and 2 and ca. 1.5 mm for case 3, therefore the total surface area (as determined by X-ray CT measurements) that maintained contact with the electrolyte and active material was measured at 1.41 and 0.96 mm^2, respectively. However, small discrepancies are likely because of the cutting procedure. To ensure uniform melting, the mass of both LKE and LCO was adjusted to optimal values of 0.3 g and 0.05 g, respectively (case 3), in an appropriate ratio to the dimensions

Table 1. Experimental details

Sample description	Case #	Temperature of electrolysis (°C)	Mass of LiCoO$_2$ (g)	Mass of LiCl-KCl (g)	Scan range (V)	Applied potential (V)	Duration of electrolysis (s)
LiCoO$_2$ + LiCl-KCl	1	450	0.05	0.5	0 to −2.7	−2.5	2,094
LiCoO$_2$ + LiCl-KCl	2	450	0.05	0.5	0 to −3	−2.75	1,937
LiCoO$_2$ + LiCl-KCl	3	450	0.05	0.3	0 to −3	−2.75	1,142
LiCl-KCl + LiCoO$_2$	4	25[a]	0.05	0.5	N/A	N/A	N/A
LiCl-KCl + Co	5	25[a]	N/A	0.5	N/A	N/A	N/A
LiCl-KCl	6	450[b]	N/A	0.5	0 to −3	N/A	N/A

[a]Sample studied at room temperature.
[b]No electrolysis performed.

of the capillary tube, compared with 0.5 g and 0.05 g (cases 1 and 2). The criteria used to optimize these values rely on the reliability of suitable electrochemical data where enough current was able to pass through the system. Unsuitable data were those which led to an uncompensated resistance profile due to the non-uniform melting of the MS. As a result, the masses of the LCO and LKE materials were optimized to ensure uniform melting of the MS. Furthermore, once the infrared (IR) spot heater had achieved a suitable working temperature (ca. 450°C), the capillary tube was further held for 10 min to allow the system to equilibrate. The temperature-time distribution for two different trials is shown in Figure S1.

A two-electrode study was employed with the use of an inert tungsten electrode and a graphite counter electrode. The scan range was kept constant between 0 and −3 V for cases 1–3. The scan ranges include the decomposition voltage of LiCl (ca. > −2.75 V), encompassing the potential window and the reoxidation potential of chloride ions to chlorine gas. Figures 2A–2C indicate the presence of coupled redox peaks. The first, labeled c1 and a1, are associated with the reduction of Co$_3$O$_4$ to CoO and the reoxidation of CoO to Co$_3$O$_4$ on the return sweep (Equation 3). Peak c1 was found to vary only by a small degree in cases 1–3 with the peak range occurring between −1.4 and −1.6 V. The general form of the CV is consistent with previously reported data.[22,23] This range was also found to agree with thermodynamic data, calculated from Equations 3 and 4, but the observation that peak c1 occurred at a far more negative potential can be justified with the increasing concentration of O^{2-} ions throughout the electrochemical reduction process (see Equations 3 and 4). As a result, case 1 necessitates a slightly more negative potential for the reduction of Co$_3$O$_4$ to CoO. The second coupled redox peak, labeled c2 and a2, describes the reduction to Co metal from CoO and the subsequent reoxidation to CoO on the return sweep (Equation 4). These observations confirm previously established work.[23] Cases 2 and 3 are presented with background CVs showing the responding current without any LCO: both CVs indicate the absence of redox peaks and only confirm the observation that the decomposition potential becomes apparent near −3 V.

$$Co_3O_4 + 2e^- \rightleftharpoons 3CoO + O^{2-}, \tag{Equation 3}$$

$$CoO + 2e^- \rightleftharpoons Co + O^{2-}. \tag{Equation 4}$$
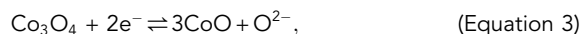
To investigate the growth of Co electrodeposits during the process, controlled potential electrolysis experiments were performed. Using the data acquired in Figures 2A–2C, a fixed potential of −2.5 V (case 1) and −2.75 V (cases 2 and 3) was chosen to induce electrodeposition of Co metal and to compare the growth of deposits using X-ray imaging, as detailed in the next section. Given the small-scale setup and the close proximity of the working and counter electrodes, minimal resistance (iR drop) is expected based on that
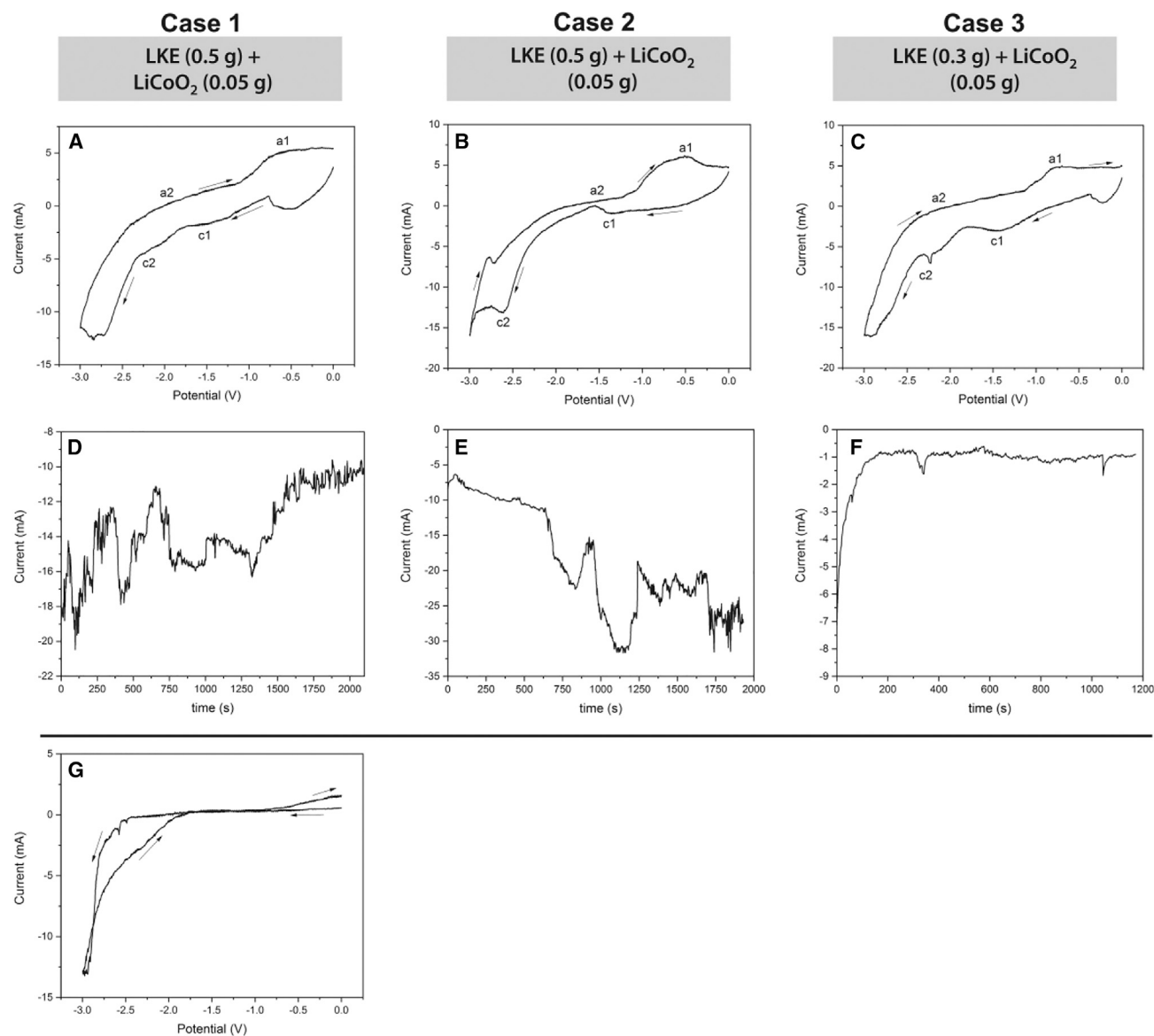
Figure 2. Electrochemical profiles which include cyclic voltammograms and chronoamperograms

(A–C) CV of $LiCoO_2$-LiCl-KCl system at 450°C using a tungsten working electrode fused within a capillary tube. The details of the experimental trials are as follows. (A) scan rate: 50 mV s^{-1}; mass of $LiCoO_2$: 0.5 g. (B) scan rate: 30 mV s^{-1}; mass of $LiCoO_2$: 0.5 g. (C) scan rate: 40 mV s^{-1}; mass of active material: 0.3 g.

(D–F) Several chronoamperograms (controlled potential electrolyses) were also performed with the following details. Fixed voltages: (D) −2.5 V; (E) −2.75 V; (F) −2.75 V. The reason the LKE was reduced in mass was due to inefficient melting of the molten salt by the IR heater. It was found that reducing the mass of the molten salt led to more uniform melting across the system.

(G) Background scan (0 to −3 V) in the absence of $LiCoO_2$ with no redox active peaks present. The mass of LKE was varied and subsequently optimized to ensure uniform melting. On the other hand, varying the mass of LCO led to a much greater difficulty in melting.

which inherently arises from the electrolyte and electrode materials. Figure 2D describes a typical current-time profile at a fixed potential of −2.5 V. During the first stage of the process, a current peak of approximately −22 mA was observed. This sharp current rise, coupled with subsequent current peaks, is evidence of the metal oxide precursor undergoing reduction, leading to the deposition of metal on the surface of the working electrode. Toward the end of the process, beyond 1,750 s, the current begins to plateau,

Cell Reports
Physical Science
Article

CellPress
OPEN ACCESS

signifying the depletion of starting material. According to previous work, the selected potential is satisfactory in reducing $LiCoO_2$ to Co metal.[23]

The current measured during the experimental trial was found to vary depending on the applied potential. Case 2, for example, differed with regard to its input parameter (with a more negative applied potential) and yielded a greater current than case 1, with a peak current of -30 mA compared with -22 mA. The theoretical charge needed to completely reduce 0.05 g of LCO is 16 C, assuming 100% current efficiency. Given that there is also incomplete reduction and by assuming the current will reach background levels, the Faradaic efficiency was found to be in excess of 90%. This is evidenced by the formation of gas bubbles and indicates the occurrence of side reactions that are occurring within the process.

X-Ray CT imaging

Following the completion of electrolysis, the capillary tube was left to cool for 10–30 min before proceeding with X-ray imaging. Thereafter, it was placed within a bespoke 3D-printed sample holder for use inside the X-ray CT scanner (Figure S2). It should be emphasized that the glass capillary tube was left intact, and all analysis was conducted without exposing the recovered materials to air, minimizing the risk of reoxidation. The scanning of the tungsten working electrode was minimized in the field of view (FOV) as a result of beam-hardening issues, and the X-ray image of the tungsten electrode was deliberately cropped and removed before continuing with data analysis. Further details of X-ray tomographic parameters can be found in Table 1. We show the microstructure of reconstructed benchmark samples (cases 4–6) (Figure 3) and reduced samples (cases 1–3) (Figures 4 and 6; Videos S1, S2, and S3). Figure 5 illustrates the X-ray histograms of brightness for each material and is a distinguishing characteristic of each phase. In our experimental study we were able to carefully study and process the X-ray images concerning the LCO powder and reduction products; however, it would be even more helpful to employ a higher-resolution X-ray CT scanner to reveal the finer details. It is well known that using 4D X-ray imaging will enable visualization of a kinetically fast process; thus we believe this approach will suit the study of dissolution of microsized LCO in the future.[32]

Figure 3 (first and second columns) shows 2D cross-sections of the LCO (denoted as case 4) and Co metal particles (denoted as case 5) within LKE eutectic at 25°C, respectively. Also, the LKE only (denoted as case 6) electrolyzed at 450°C is presented in Figure 3 (third column). At room temperature, the density of elemental Co metal is 8.90 g cm^{-3} and the density of LCO is 4.79 g cm^{-3}, whereas the density of LiCl and KCl is 2.07 g cm^{-3} and 1.98 g cm^{-3}, respectively. In Figures 3B and 3E, since elemental Co is more than four times denser than the respective electrolyte, it will absorb more of the X-ray photons and will consequently appear as the brightest particles. In Figure 5, a strong peak (grayscale range from 200 to 255) representing the elemental Co is observed at the right end of the blue line (case 5). In Figures 3A and 3C, the LCO phase will be less bright than the Co phase, since the LCO has a lower density than Co. Indeed, the Co signal strength of case 4 (red line) is slightly lower than that of case 5 (blue line) at the right end of each profile in Figure 5. In contrast, the gas produced has the lowest density and appears as the darkest region; therefore, the corresponding signal range will be located at the left end of the X-ray histogram, ranging from 0 to ca. 65. The remaining (gray) particles in this sample can be classified as the LKE eutectic, and their signal is located in the middle range of the X-ray histogram. Figures 3C and 3F show the LKE structure (light gray) without active materials (LCO or Co)
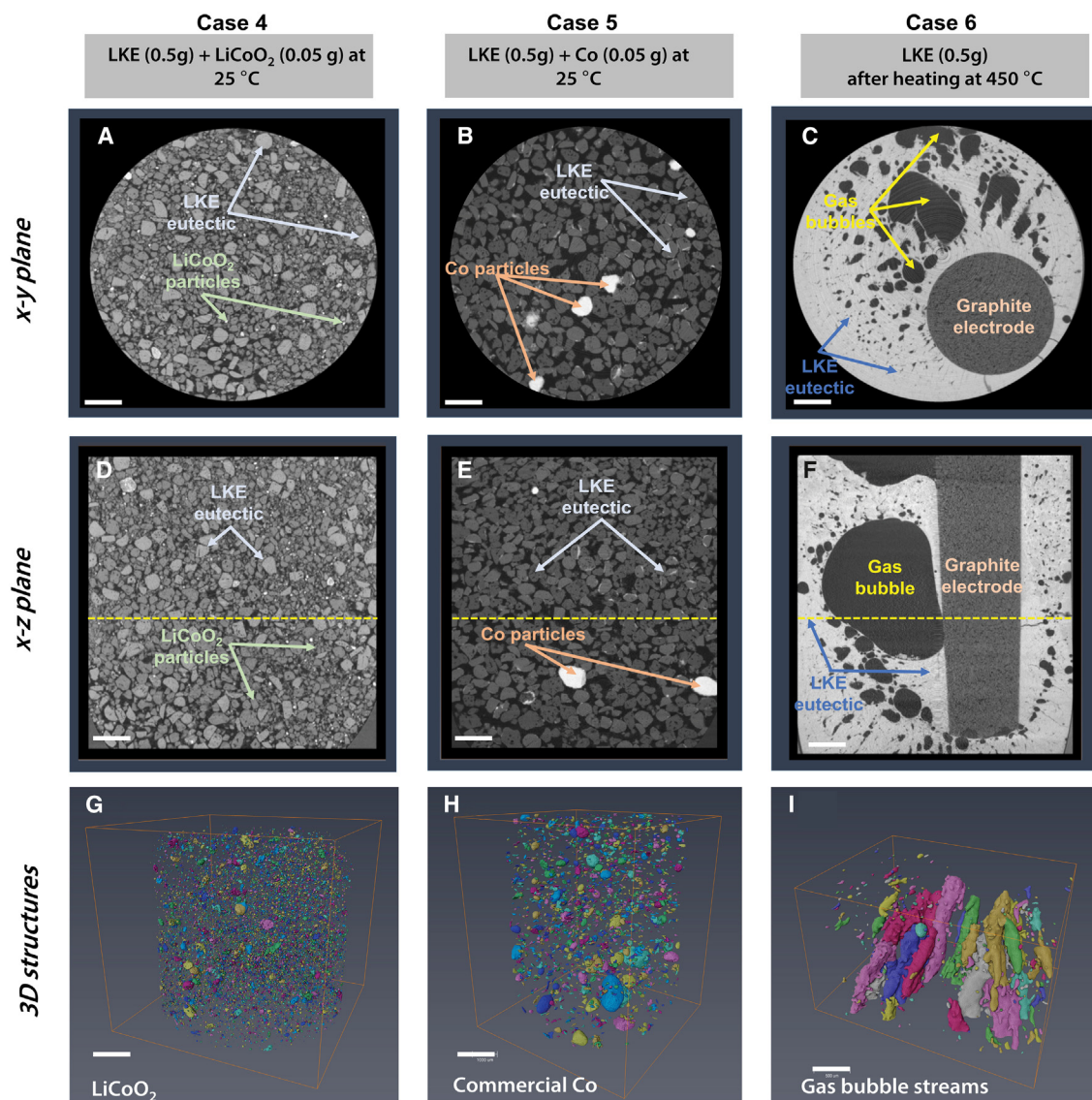
Figure 3. X-ray CT images of the benchmark samples

(A–I) (A, D, and G) Case 4: LiCl-KCl (LKE, 0.5 g) with LiCoO$_2$ (0.05 g) at 25°C prior to heating. (B, E, and H) Case 5: LKE (0.5 g) with commercially obtained Co particles (0.05 g) at 25°C. The commercially obtained Co was deliberately added into LKE salts to identify Co image contrast for subsequent reduction samples. (C, F, and I) Case 6: LKE (0.5 g) only electrolyzed at 450°C indicating the presence of a graphite electrode and gas bubbles. 2D cross-sections at x-y planes (A–C) and x-z planes (D–F) were selected in the middle of FOV to show the overall look, and 3D microstructure of separated (G) LiCoO$_2$ particles, (H) commercial Co particles, and (I) gas channels before electrolysis (with each particle/gas assigned a different color to its neighboring particle/gas).

The locus of the orthoslices in the x-y plane is indicated by the yellow dashed line in the x-z plane. Scale bars, 1 mm.

after electrolysis at 450°C to complement the prior cyclic voltammetry studies (Figures 2B and 2C). Clearly there is no bright phase appearing in the system, and no signal above a grayscale value of 225 is detected in the X-ray histogram (black line in Figure 5), both confirming the absence of Co metal.

It can be clearly seen that the commercially obtained LCO has a smaller particle size than the commercially obtained Co particles, while the particle size of LKE eutectic in cases 4 and 5 is identical at 25°C. Meanwhile, there are many generated gas bubbles, with diameters up to 2 mm, observed within the salt near the counter
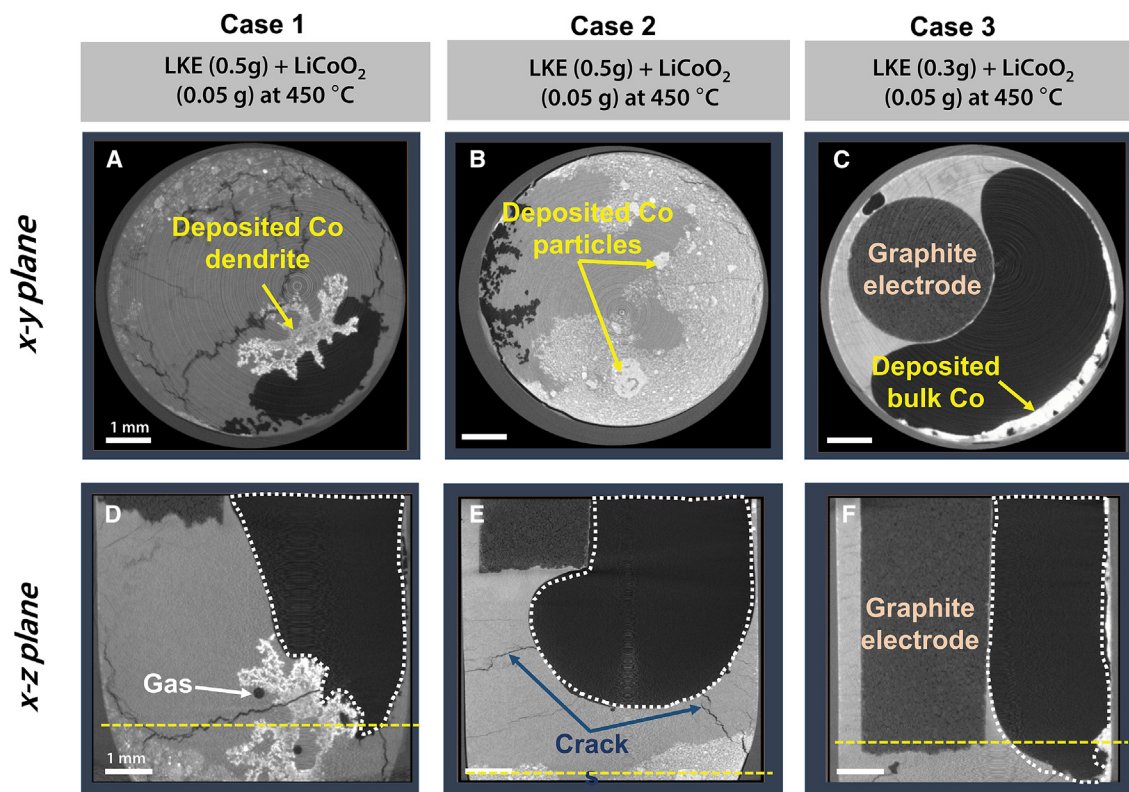
CellPress
OPEN ACCESS

Figure 4. 2D X-ray CT images of the electrodeposited samples after electrolysis treatment at 450°C

(A–F) (A and D) Case 1: LKE (0.5 g) with $LiCoO_2$ (0.05 g) after heating at 450°C. (B and E) Case 2: LKE (0.5 g) with $LiCoO_2$ (0.05 g) after heating at 450°C. (C and F) Case 3: LKE (0.3 g) with $LiCoO_2$ (0.05 g) after heating at 450°C. Reconstructed x-y (A–C) and x-z (D–F) planes of recovered Co metal with LKE showing different microstructures and morphologies in 2D. The locus of the orthoslices in the x-y plane is indicated by the yellow dashed line in the x-z plane. Scale bars, 1 mm.

electrode during electrolysis, visible in 2D. For visualization purposes, each gas bubble was assigned a different color after image binarization. Interestingly, the gaseous products in Figure 3I appear as long streams with a length up to 1.5 mm, demonstrating how X-ray CT imaging can be used to improve our understanding of the 3D microstructure. The production of these gases may, especially in copious amounts, lead to a "blinding effect" and as a result increase the electrolyte resistance and noise generation in the electrochemical signal. On the other hand, using destructive characterization techniques will prevent any understanding of this gas evolution, and the genuine shape of the bubbles can only be retrieved using X-ray CT. The relationship between gaseous bubble evolution and the electrochemical signal-related "blinding effect" will be discussed in detail in our subsequent *in situ* study. To this end, cases 4 and 5 are images of our commercially obtained starting and final product material, and case 6 illustrates the MS medium in the absence of a precursor.

Figure 4 illustrates the 2D microstructure of recovered Co metal and other material phases following electrolysis at 450°C at different processing times and mass ratios in the entire FOV. In particular, in all three of the reduced samples the recovered Co metal (yellow arrows) exhibited three different morphological types, which we describe as dendrite (case 1), particles (case 2), and bulk shapes (case 3). These deposited Co particles formed either near the bottom of the capillary, in close proximity to the working electrode, or next to the tube wall (indicated by the yellow
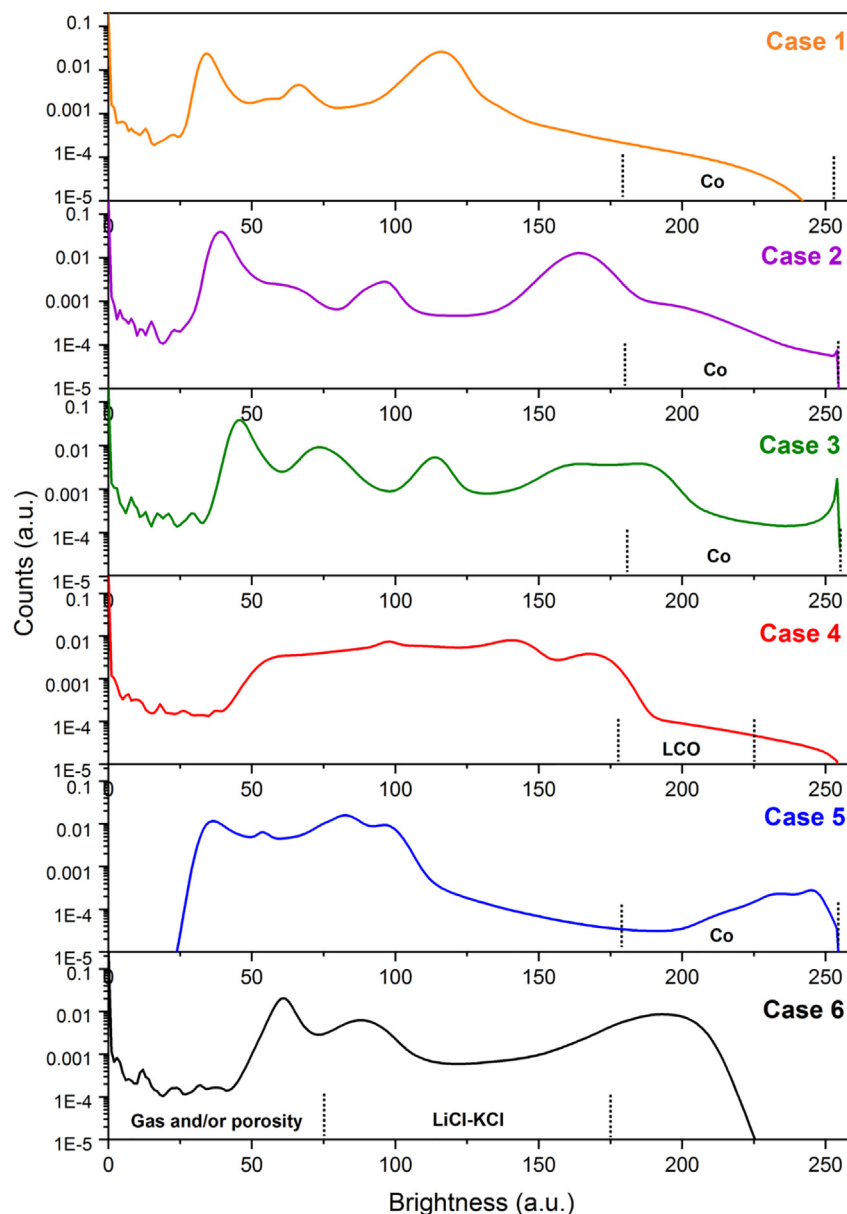
Figure 5. Histograms of brightness

Case 1: LKE (0.5 g) with $LiCoO_2$ (0.5 g) after heating at 450°C. Case 2: LKE (0.5 g) with $LiCoO_2$ (0.5 g) after heating at 450°C with an applied potential different from that of case 1. Case 3: LKE (0.3 g) with $LiCoO_2$ (0.5 g) after heating at 450°C. Case 4: LKE (0.5 g) with $LiCoO_2$. Case 5: LKE (0.5 g) with Co metal particles (0.05 g). Case 6: LKE (0.5 g) only.

arrows), or a combination of all three. Interestingly, the recovered Co deposits seem to be naturally segregated from this mixture after electrolysis. This means much less effort and energy will be required for subsequent Co separation and extraction. Our experiments benefit from a large FOV and a relatively high voxel resolution at 5 μm.

Using the benchmark samples, the microstructure of the MS before (case 6) and after (cases 1–3) electrolysis can be compared. The presence of cracks and gas bubbles (white arrows) are observed within the salt mixture in all samples (cases 1–3). It seems that less gas has been generated when one compares cases 1–3 against case 6.

Here, we speculate that the formation of such cracks and fissures could be attributed to (1) the production of CO_2 gas and (2) the contraction of the MS after cooling. In Figure 5, the presence of gas is demonstrated by the formation of the first peaks at low-grayscale values (ca. 50), which becomes more apparent after heating (orange, purple, and green lines). Moreover, in each case a large black region (outlined with a dashed white line) is observed next to the graphite counter electrode. During chronoamperometric experiments, we visually observed the gas bubble movement within this region. Such phenomena might be strongly correlated with the internal gas flow, and this merits further investigation by ultrafast X-ray imaging.

In Figure 6 and Videos S1, S2, and S3, the 3D microstructure of recovered Co metal following electrolysis at 450°C is illustrated. In the first row (Figures 6A–6C), 3D volume renderings of MS (view set as 70% transparent) are superimposed with the recovered Co depositions (labeled in yellow). 3D images illustrate the distribution of the newly formed Co depositions as well as the salt mixture, strengthening the prior 2D observations. To directly characterize the Co under various electrolysis conditions, the salt mixture is deliberately masked and Co depositions are only displayed in Figures 6D–6F (second row). It is observed that multiple morphologies can coexist in an individual case. For instance, in case 1 (electrolysis time is 2,094 s where the mass ratio is 1:10), the coexistence of recovered Co dendrites and Co particles are observed in Figures 6A and 6D. Two enlarged regions of interest (ROIs) can be extracted from the whole FOV, showing a non-uniform dendrite deposit (Figure 4G) and particle (Figure 6H) features, respectively. It should be mentioned that in previous work on the electrochemical reduction of UCl_3 in LKE, the formation of uranium dendrites has been observed; this was found to impede the electrolytic process as its formation was found to slow the uranium deposition.[33] Indeed, our study also yields a similar result, since case 1 takes the longest time, 2,094 s, to recover the Co materials.

The commercially obtained Co particles (case 5, Figure 3H) were compared with the recovered Co particles (case 1, Figure 6H) via particle size distribution (PSD) analysis. Initially, individual Co particles were separated and assigned different colors with respect to their neighboring particle. The diameter (Φ) and sphericity (Ψ) of recovered Co (Figures 7A and 7B), commercially obtained LCO (Figures 7C and 7D), and commercially obtained Co (Figures 7E and 7F) samples are plotted with PSD data. The Ψ is a measure of sphericity, and when the value $\Psi = 1$ the object under observation can be classified as a perfect sphere. It was found that the recovered Co has a much rounder and smoother shape (greater sphericity) than the commercially obtained Co sample, according to statistical analysis. The recovered Co (mean diameter of 58.4 μm) has a diameter similar to that of the commercially obtained Co (mean diameter of 54.2 μm), as shown in Figures 7A and 7E. Also, the higher sphericity (80% > 0.85) of the recovered Co particles implies that they have a larger volume-specific surface area (S) than the commercially obtained particles (80% < 0.75). This is verified by the quantification as $S_{recovered\ Co}$ is 0.037 μm^{-1} for case 1, whereas $S_{commercially\ obtained\ Co}$ is 0.027 μm^{-1} for case 5. The specific surface area can be calculated using the equation $S_v = A/V$, where A and V denote the Co surface area and Co volume (enclosed by surface area), respectively. The reason for comparing the recovered (electrolyzed) Co particles with commercially obtained Co particles is to evaluate the morphological characteristics produced. We are then able to determine whether they are suitable for secondary use, as the specific surface area and particle size affect the material performance. The X-ray CT data were used for the above volume quantification.
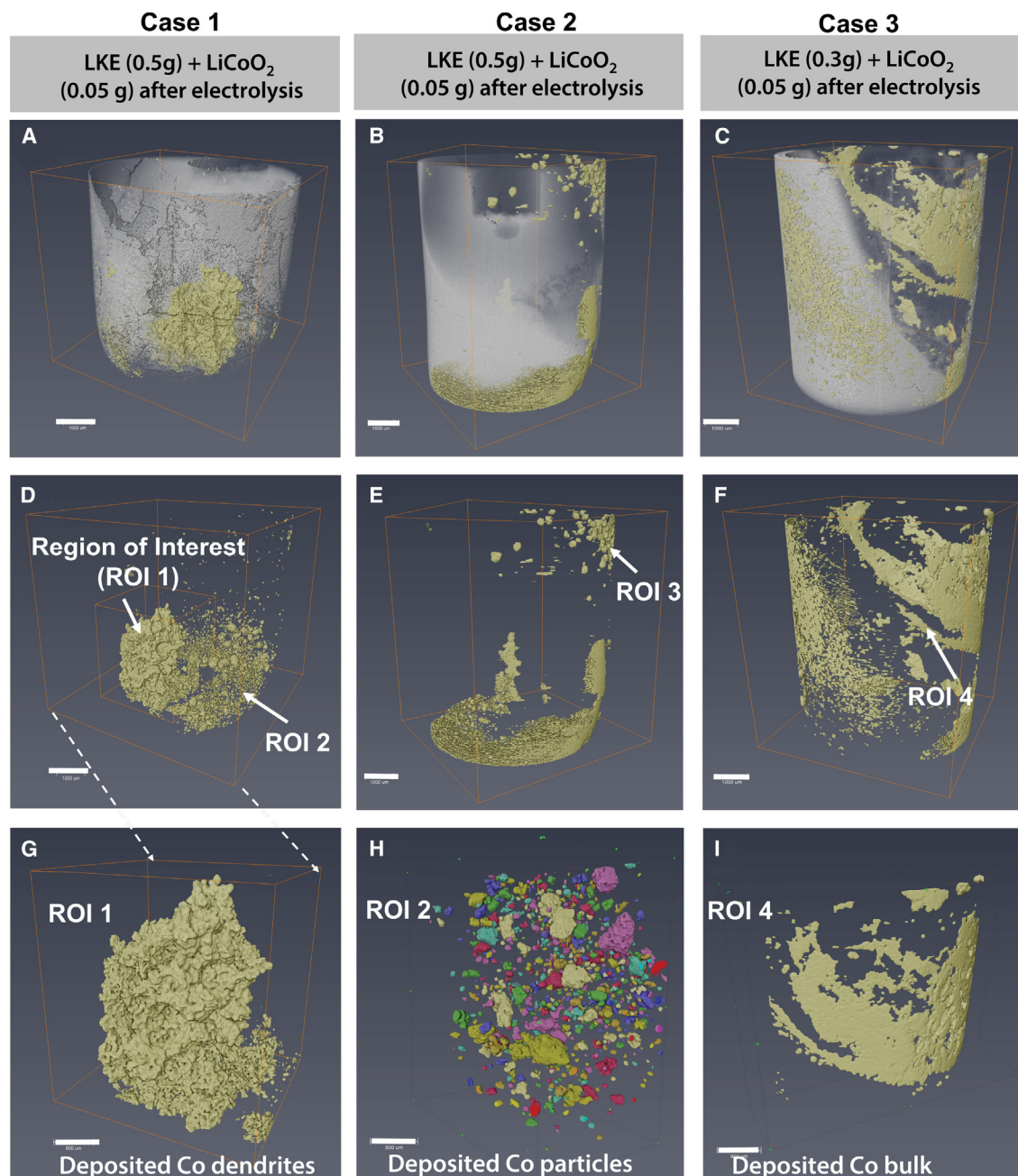
Figure 6. 3D X-ray CT images of the electrodeposited samples after electrolysis treatment at 450°C

(A–C) Different morphologies of the recovered Co metal under various processing times and mass ratio. The volume renderings within the entire FOV, where the LKE materials are rendered as semi-transparent (70%) with the recovered Co materials (assigned yellow).

(D–I) Correspondingly, in (D) to (F) the recovered Co metal (the LKE materials are masked) is displayed to show its Co distribution. Two magnified ROI regions from (D) show that both the deposited Co dendrites in ROI 1 (H) and Co particles in ROI 2 (I) are observed after treatment. Another enlarged region (ROI 4) (I) shows Co bulk from (F).

Scale bars, 1 mm (A–F), 600 μm (G), 500 μm (H), and 900 μm (I).

The formation of bulk Co depositions is observed in case 2 (electrolysis time is 1,937 s, the mass ratio is 1:10) and case 3 (electrolysis time is 1,142 s, the mass ratio is 1:6). In particular, a screw-like Co microstructure was observed in three dimensions, which was unevenly distributed near the inner edge of the capillary tube, as shown in
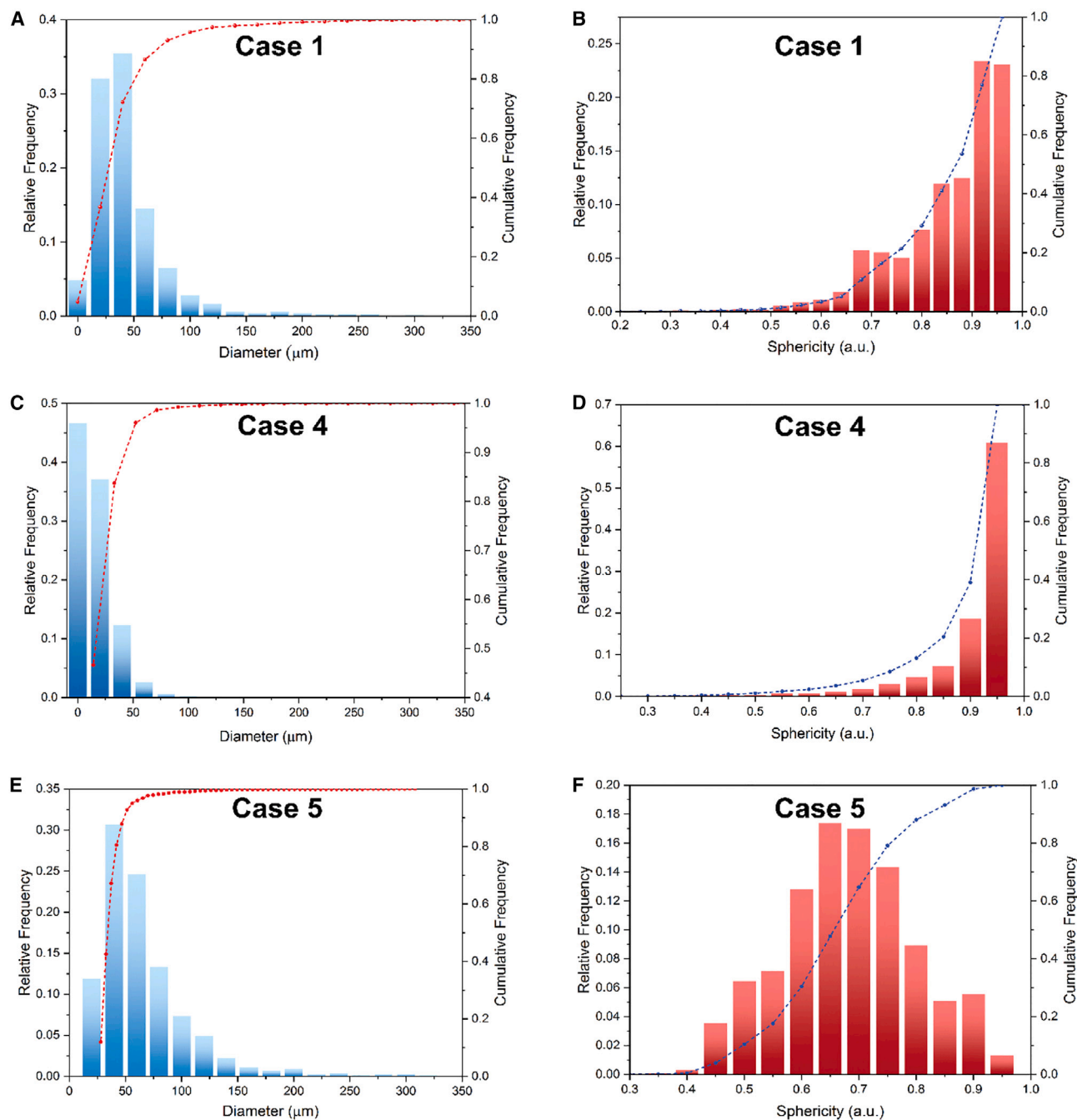
Figure 7. The quantification of particles includes particle diameter and sphericity

(A–F) (A, C, and E) Particle diameter. (B, D, and F) Sphericity. (A) and (B) are the recovered Co metal particles. (C) and (D) are the commercially obtained LiCoO$_2$ particles. (E) and (F) are the commercially obtained Co particles.

Figures 6F and 6I. It is difficult to perform the PSD analysis for the above two cases, since the metal depositions have coalesced after electrolysis. Despite this difficulty, two typical local regions (ROI 3 and ROI 4, indicated by arrows in Figures 6E and 6F) were extracted from the entire FOV for structural thickness quantification. The morphologies of layer-like Co metals are included in ROI 3 and ROI 4, which are selected from case 2 and case 3, respectively. Figure 8 illustrates 2D (Figures 8A and 8B) and
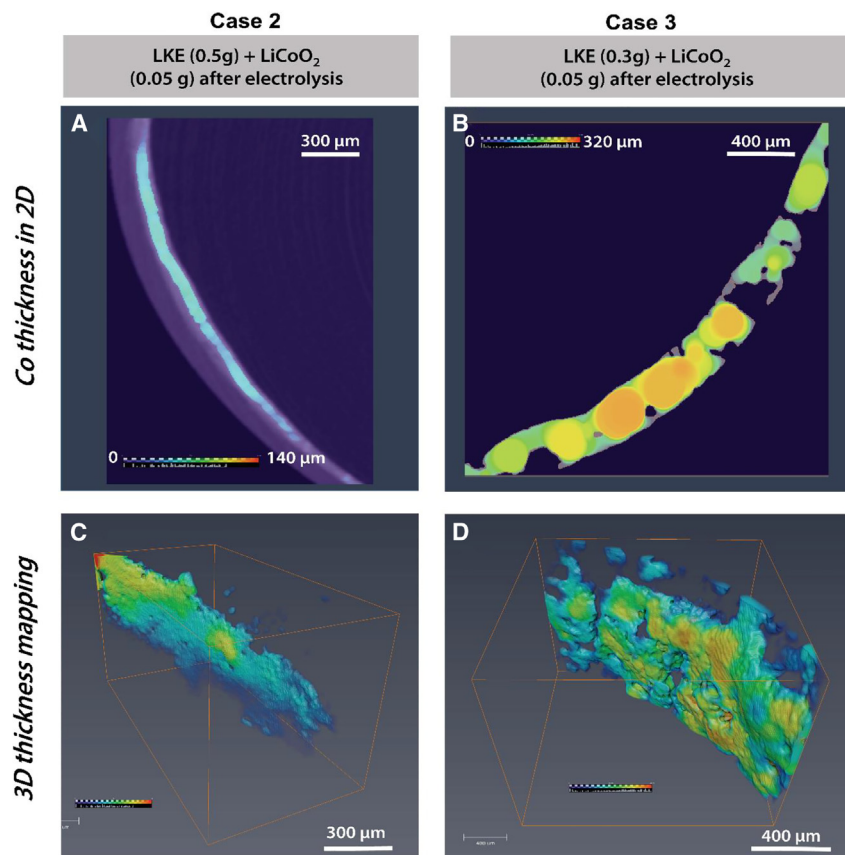
Figure 8. Mapping the recovered Co thickness
(A–D) The quantifications are selected from ROI 3 (A and C) and ROI 4 (B and D). 2D (A and B) and associated 3D (C and D) thickness distribution of the recovered Co metal. The color bars represent thickness ranges 0–140 and 0–320 μm, respectively.

associated 3D (Figures 8C and 8D) normalized thickness mappings for recovered Co bulk. The recovered Co bulk, as well as its thickness distribution at the local region, can be represented together (Figure 8). It should be noted that the color bar in Figure 8 represents the microstructure thickness (Co metal deposition) near the capillary tube. For instance, a uniform layer of recovered Co metal with an average thickness of 70 μm is deposited on the inner tube wall, as shown in Figures 8A and 8C, while the Co deposition with a higher thickness value (ranging from 0 to 320 μm, average of 225 μm) is displayed in Figures 8B and 8D.

Also, it should be noted that the uneven thickness distribution in case 3 is presumably attributed to the incomplete agglomeration of Co particles due to the shortest electrolysis time (1,142 s). This could be supported both with X-ray images and prior electrochemical results. For case 3, we observed the occurrence of incomplete merging of Co particles in Figure 8B and the lower current from chronoamperometry in Figure 2F. In Figure 8 case 2 has a much thinner thickness than case 3, suggesting that case 2 may have a lower mass of recovered Co compared with case 3. By comparing the purple line (case 2) with the green line (case 3) in Figure 5, we see an obvious very sharp peak at the right end of the X-ray histogram and a higher signal intensity for case 3, indirectly indicating that case 3 created more Co product than case 2. This peak signal in case 3 is identical to the benchmark (case 5), suggesting the best recovery scenario among all three cases. Hence, increasing the ratio of LCO to LKE MS (i.e., in this study from 1:10 to

1:6) may help generate a greater quantity of recovered Co metal, which improves the recovery efficiency of Co from LCO. These results imply that the metal oxide-to-salt ratio can significantly affect the LCO reduction process because the potential (a constant voltage of 2.75 V) and temperature (450°C) are identical.

This research shows that the microstructure can be manipulated and tailored under different conditions. According to the predominance diagram of the Li-Co-O-Cl system at 500°C (Figure S3), the voltage and oxide ion concentration play a crucial role in determining the completion of the electrochemical process. For this reason, experiments were carried out using two voltages (−2.5 and −2.75 V) to correlate the final microstructures. *In situ* and *in operando* X-ray imaging and diffraction techniques will be the next set of steps to determine the dynamic evolution of chemical and microstructures across the entire recovery process. This will advance an already robust system with high efficiency and ultimately lead to a sustainable approach to the recovery of critical materials.

Microstructural characterization of the electrochemical reduction of $LiCoO_2$ to Co within an LKE MS has been performed using X-ray imaging. Base case comparisons allow different components ($LiCoO_2$, Co, LKE, and gas) to be identified based on their X-ray attenuation (brightness). The approach offers new insight into understanding and optimizing process conditions and electrochemical cell design for pyro-electrochemical processing and seeks to advance work conducted by Zhang et al. by utilizing a lower-temperature MS eutectic and providing X-ray CT images of the final obtained product morphology.[22] The major findings include the following.

1. Three different morphological types of recovered Co product have been observed in 3D; namely, dendrite extensions, particles and bulk shapes at various potentials, and differing lengths of electrolysis. The non-uniformity of the particles might be attributed to the presence of different crystal structures.[22]
2. Under a lower potential of −2.5 V, recovered Co particles have a much rounder shape (greater sphericity) with a smaller particle size (average of 54 μm) than the commercially obtained Co particles (average of 80.5 μm).[22,23]
3. By increasing the potential (i.e., from −2.5 to −2.75 V) we are much more likely to generate a greater quantity of recovered Co metal.

For the first time, we have designed a borosilicate glass capillary tube (10 cm in length) to visualize the changes in morphology using an industrial X-ray CT scanner. An X-ray CT scanner offers a non-destructive approach to 3D microstructure visualization of recovered metal deposits. By using this we have realized that the gas production which occurs at the counter electrode surface will lead to operational consequences where there will be a much greater electrolyte resistance. As a result, this will significantly diminish the efficiency of the process and affect the potential at which the process occurs.

Moreover, our design offers a 2-fold benefit; first it allows for the visualization of metal oxide particles undergoing reduction non-invasively and, since it has found merit in this application, it also opens up the possibility of transfer to other applications and systems. Our electrochemical cell is both strong enough to withstand high temperatures (∼450°C) and small enough to sit within a sample holder for X-ray scanning. This contribution is the first major step in elucidating the electrochemical

reduction pathway of metal oxide particles using X-ray CT, and we expect to transfer this technology to other battery materials (i.e., NMC and NCA).

EXPERIMENTAL PROCEDURES

Resource availability

Lead contact
Further information and requests for resources should be directed to and will be fulfilled by the lead contact, Dan J.L. Brett (d.brett@ucl.ac.uk).

Materials availability
This study did not generate new unique reagents.

Data and code availability
All underlying data are provided in the article and supplemental information, or are available from the authors upon request. This study did not generate any code.

Preparation of electrochemical cell
The electrochemical reduction process was conducted within a borosilicate capillary glass tube (internal diameter 6 mm). Within this design, a tungsten rod (99.95% metals basis, diameter 1.5 mm, Alfa Aesar) was covered by borosilicate glass, which expands, into a narrow opening to allow for the tip of the electrode to be exposed and used as the working electrode. A high-density graphite rod (99.9995% metal basis, diameter 3.05 mm, 0.2/0.5 cm depth in electrolyte, Alfa Aesar) was used as a counter electrode, inserted through a Suba-Seal at the top end of the capillary tube. The $LiCoO_2$ and LiCl-KCl materials were placed within the capillary tube within a moisture (<0.5 ppm) and oxygen-free (<0.5 ppm) glovebox, which remained under constant argon gas circulation. Anhydrous lithium chloride (Extra Pure, SLR, Fisher Scientific) and potassium chloride (Certified AR for Analysis, Fisher Scientific) were initially vacuum dried (removing residual moisture) to 150°C for 24 h, and a eutectic mixture (either 0.3 or 0.5 g) was prepared by mixing (LiCl) 59 mol % and (KCl) 41 mol %, respectively. Commercially obtained lithium cobalt oxide (97%, Alfa Aesar) was added to the LKE mixture as a surrogate for spent battery material. The mass of LCO was 0.05 g in all experimental trials. A background CV was also collected in the absence of active material (LCO). Commercially obtained Co powder (99.8% metals basis, Alfa Aesar) mixed with LKE was also studied in this work as a point of comparison and as a potential precursor for battery manufacture.

Heating procedure and rig assembly
An infrared (IR) spot heater (Model 4150, Precision Control Systems Inc.) was mounted within a fixed strut assembly (RS Components) to support the weight of the heater at a height of 40 cm from the benchtop surface. This heater, comprising a tungsten filament emitter, was connected to a supply of compressed air (Zero grade, BOC), with a flow rate of approximately 55 L min^{-1}, to maintain suitable operating conditions during the heating process and prolong instrument life. The heating of the capillary tube occurred at a rate of 15°C min^{-1} to ca. 450°C using a variable AC power supply. A K-type thermocouple was positioned near the capillary tube to measure temperature, and all thermal data were recorded using a data logger (TC-08, Pico Technology, UK). For further details, see Figure S2.

Electrochemical measurements
All electrochemical measurements (cyclic voltammetry and chronoamperometry) were performed on a two-electrode system consisting of a working (tungsten) and counter (graphite) electrode. Using a PC-controlled potentiostat (ref. 3000, Gamry

Cell Reports Physical Science Article

CellPress
OPEN ACCESS

Table 2. X-ray tomographic imaging acquisition parameters

Sample description	Case #	Resolution (μm)	Voltage (kV)	Power (W)	Exposure time (s)	No. of projections	FOV (mm^2)
All samples	1–6	5	90	5	1	3,185	10 × 10

Instruments, USA), CVs were recorded at a scan rate within the region of 30–50 mV s^{-1}, and the potential range was measured between 0 and −3 V at ca. 450°C for all trials. During the electrolysis, a minor fluctuation in temperature was observed but this was not found to impede the electrolytic process (Figure S1). Thereafter, chronoamperometric measurements were conducted and suitable potentials were applied, having been deduced from the CVs. A constant voltage of −2.5 (case 1) and −2.75 V (cases 2 and 3) was applied to ensure complete reduction to the metal, avoiding the decomposition voltage of LiCl (ca. −3 V).

X-ray computed tomography

An X-ray CT scanner (Nikon XT 225, Nikon Metrology, UK) employing a tungsten target was used to investigate the electrolyzed and control samples for which the voltage and power were set to 90 kV and 5 W, respectively. The X-ray experimental setup and 3D-printed holder (Ultimaker S3) are shown in Figure S2. Using a 1-mm Cu filter, 3,185 projections were collected per tomogram with an exposure time of 1 s per projection. A voxel resolution at ca. 5 μm with an FOV of ca. 10 × 10 mm^2 was provided by using a 2,028 × 2,028 pixel CCD camera detector. Both the working (tungsten-based) and the counter (graphite) electrodes were maintained within the FOV. Identical X-ray parameters were used for all samples, the details of which are summarized in Table 2.

X-ray image processing

The raw X-ray projections were reconstructed using Nikon CT Pro 3D software (version XT 4.4.4, Nikon Metrology, Tring, UK). All undesirable regions from the reconstructed tomograms were cropped and then converted from 16-bit to 8-bit images before importing into Avizo 2019.4 (Thermo Fisher Scientific, France) for image processing. The "undesirable" regions denote the working electrode (tungsten metal with a high density), which leads to beam-hardening artifacts. An anti-diffusion filter was applied to remove the ring artifacts and thus improve image quality prior to segmentation. Features <50 voxels were removed, and the separate objects module in Avizo was used to isolate the Co particles for label analysis. Thereafter, image quantification, including diameter, sphericity, and thickness of deposited Co layers, was performed. The thickness module in Avizo was used to map the thickness distribution of recovered Co in 3D.

SUPPLEMENTAL INFORMATION

Supplemental information can be found online at https://doi.org/10.1016/j.xcrp.2023.101333.

CellPress
OPEN ACCESS

Cell Reports
Physical Science
Article

AUTHOR CONTRIBUTIONS

M.M. and W.D.: investigation, methodology, verification, formal analysis, and writing. L.R.: investigation. S.W. and A.H.J.: supervision. P.R.S. and D.J.L.B.: conceptualization, supervision, project administration, and funding acquisition.

DECLARATION OF INTERESTS

The authors declare no competing interests.

REFERENCES

1. Alhindawi, R., Nahleh, Y.A., Kumar, A., and Shiwakoti, N. (2020). Projection of greenhouse gas emissions for the road transport sector based on multivariate regression and the double exponential smoothing model. Sustainability 12, 1–18. https://doi.org/10.3390/su12219152.

2. Velázquez-Martínez, O., Valio, J., Santasalo-Aarnio, A., Reuter, M., and Serna-Guerrero, R. (2019). A critical review of lithium-ion battery recycling processes from a circular economy perspective. Batteries 5, 68. https://doi.org/10.3390/batteries5040068.

3. (2019). Recycle spent batteries. Nat. Energy 4, 253. https://doi.org/10.1038/s41560-019-0376-4.

4. Gielen, D., Gorini, R., Wagner, N., Leme, R., and Prakash, G. (2020). Global Renewables Outlook: Energy Transformation 2050.

5. Piçarra, A., Annesley, I.R., Otsuki, A., and de Waard, R. (2021). Market assessment of cobalt: identification and evaluation of supply risk patterns. Resour. Pol. 73, 102206. https://doi.org/10.1016/j.resourpol.2021.102206.

6. van den Brink, S., Kleijn, R., Sprecher, B., and Tukker, A. (2020). Identifying supply risks by mapping the cobalt supply chain. Resour. Conserv. Recycl. 156, 104743. https://doi.org/10.1016/j.resconrec.2020.104743.

7. Harper, G., Sommerville, R., Kendrick, E., Driscoll, L., Slater, P., Stolkin, R., Walton, A., Christensen, P., Heidrich, O., Lambert, S., et al. (2019). Recycling lithium-ion batteries from electric vehicles. Nature 575, 75–86. https://doi.org/10.1038/s41586-019-1682-5.

8. Gao, W., Song, J., Cao, H., Lin, X., Zhang, X., Zheng, X., Zhang, Y., and Sun, Z. (2018). Selective recovery of valuable metals from spent lithium-ion batteries – process development and kinetics evaluation. J. Clean. Prod. 178, 833–845. https://doi.org/10.1016/j.jclepro.2018.01.040.

9. Vieceli, N., Casasola, R., Lombardo, G., Ebin, B., and Petranikova, M. (2021). Hydrometallurgical recycling of EV lithium-ion batteries: effects of incineration on the leaching efficiency of metals using sulfuric acid. Waste Manag. 125, 192–203. https://doi.org/10.1016/j.wasman.2021.02.039.

10. Zhang, P., Yokoyama, T., Itabashi, O., Suzuki, T.M., and Inoue, K. (1998). Hydrometallurgical process for recovery of metal values from spent lithium-ion secondary batteries. Hydrometallurgy 47, 259–271. https://doi.org/10.1016/S0304-386X(97)00050-9.

11. Ferreira, D.A., Prados, L.M.Z., Majuste, D., and Mansur, M.B. (2009). Hydrometallurgical separation of aluminium, cobalt, copper and lithium from spent Li-ion batteries. J. Power Sources 187, 238–246. https://doi.org/10.1016/j.jpowsour.2008.10.077.

12. Swain, B., Jeong, J., Lee, J., Lee, G.-H., and Sohn, J.-S. (2007). Hydrometallurgical process for recovery of cobalt from waste cathodic active material generated during manufacturing of lithium ion batteries. J. Power Sources 167, 536–544. https://doi.org/10.1016/j.jpowsour.2007.02.046.

13. Makuza, B., Tian, Q., Guo, X., Chattopadhyay, K., and Yu, D. (2021). Pyrometallurgical options for recycling spent lithium-ion batteries: a comprehensive review. J. Power Sources 491, 229622. https://doi.org/10.1016/j.jpowsour.2021.229622.

14. Jin, H., Zhang, J., Wang, D., Jing, Q., Chen, Y., and Wang, C. (2022). Facile and efficient recovery of lithium from spent LiFePO4 batteries via air oxidation–water leaching at room temperature. Green Chem. 24, 152–162. https://doi.org/10.1039/D1GC03333F.

15. Lv, W., Wang, Z., Cao, H., Sun, Y., Zhang, Y., and Sun, Z. (2018). A critical review and analysis on the recycling of spent lithium-ion batteries. ACS Sustain. Chem. Eng. 6, 1504–1521. https://doi.org/10.1021/acssuschemeng.7b03811.

16. Cardarelli, F., and Dube, J. (2007). Method for Recycling Spent Lithium Metal Polymer Rechargeable Batteries and Related Materials. Patent, US7192564B2.

17. Xu, L., Chen, C., and Fu, M.-L. (2020). Separation of cobalt and lithium from spent lithium-ion battery leach liquors by ionic liquid extraction using Cyphos IL-101. Hydrometallurgy 197, 105439. https://doi.org/10.1016/j.hydromet.2020.105439.

18. Barnett, R., Kilby, K.T., and Fray, D.J. (2009). Reduction of tantalum pentoxide using graphite and tin-oxide-based anodes via the FFC-Cambridge process. Metall. Mater. Trans. B 40, 150–157. https://doi.org/10.1007/s11663-008-9219-6.

19. Abdulaziz, R., Brown, L.D., Inman, D., Shearing, P.R., and Brett, D.J.L. (2017). Electrochemical reduction of tungsten oxide in LiCl-KCl molten salt eutectic using the fluidised cathode process. Electrochim. Acta 226, 18–28. https://doi.org/10.1016/j.electacta.2016.12.114.

20. Delpech, S. (2013). In Molten Salts Chemistry From Lab to Applications, F. Lantelme and H.B.T. Groult, eds. (Elsevier), pp. 497–520.

21. Chen, G., Fray, D., and Farthing, T. (2000). Direct electrochemical reduction of titanium dioxide in molten calcium chloride. Nature 407, 361–364. https://doi.org/10.1038/35030069.

22. Zhang, B., Xie, H., Lu, B., Chen, X., Xing, P., Qu, J., Song, Q., and Yin, H. (2019). A green electrochemical process to recover Co and Li from spent LiCoO2-based batteries in molten salts. ACS Sustain. Chem. Eng. 7, 13391–13399. https://doi.org/10.1021/acssuschemeng.9b02657.

23. Mirza, M., Abdulaziz, R., Maskell, W.C., Tan, C., Shearing, P.R., and Brett, D.J.L. (2021). Recovery of cobalt from lithium-ion batteries using fluidised cathode molten salt electrolysis. Electrochim. Acta 391, 138846. https://doi.org/10.1016/j.electacta.2021.138846.

24. Liu, Y.-L., Yan, Y.-D., Han, W., Zhang, M.-L., Yuan, L.-Y., Liu, K., Ye, G.-A., He, H., Chai, Z.-F., and Shi, W.-Q. (2013). Extraction of thorium from LiCl–KCl molten salts by forming Al–Th alloys: a new pyrochemical method for the reprocessing of thorium-based spent fuels. RSC Adv. *3*, 23539–23547. https://doi.org/10.1039/C3RA43292K.

25. Zou, X., Ji, L., Lu, X., and Zhou, Z. (2017). Facile electrosynthesis of silicon carbide nanowires from silica/carbon precursors in molten salt. Sci. Rep. *7*, 1–9. https://doi.org/10.1038/s41598-017-10587-5.

26. Yoo, B., Ri, V., Kwon, S., Cho, S., Nersisyan, H.H., Park, K.-T., and Lee, J. (2021). Direct electrochemical reduction of natural ilmenite into ferrotitanium alloys in a molten salt of LiCl-Li$_2$O. J. Electrochem. Soc. *168*, 26513. https://doi.org/10.1149/1945-7111/abe291.

27. Jee, Y.T., Park, M., Cho, S., and Yun, J.-I. (2019). Selective morphological analysis of cerium metal in electrodeposit recovered from molten LiCl-KCl eutectic by radiography and computed tomography. Sci. Rep. *9*, 1–10. https://doi.org/10.1038/s41598-018-38022-3.

28. Bale, H.A., Haboub, A., MacDowell, A.A., Nasiatka, J.R., Parkinson, D.Y., Cox, B.N., Marshall, D.B., and Ritchie, R.O. (2013). Real-time quantitative imaging of failure events in materials under load at temperatures above 1,600 °C. Nat. Mater. *12*, 40–46. https://doi.org/10.1038/nmat3497.

29. Liu, X., Ronne, A., Yu, L.-C., Liu, Y., Ge, M., Lin, C.-H., Layne, B., Halstenberg, P., Maltsev, D.S., Ivanov, A.S., et al. (2021). Formation of three-dimensional bicontinuous structures via molten salt dealloying studied in real-time by in situ synchrotron X-ray nano-tomography. Nat. Commun. *12*, 3441. https://doi.org/10.1038/s41467-021-23598-8.

30. Handong, J., Zhaoliang, Q., Shuqiang, J., Yang, G., Shijie, L., Wei-Li, S., Haosen, C., Hongmin, Z., Rongqi, Z., and Daining, F. (2022). A 4D x-ray computer microtomography for high-temperature electrochemistry. Sci. Adv. *8*, eabm5678. https://doi.org/10.1126/sciadv.abm5678.

31. Brown, L.D., Abdulaziz, R., Tjaden, B., Inman, D., Brett, D.J.L., and Shearing, P.R. (2016). Investigating microstructural evolution during the electroreduction of UO$_2$ to U in LiCl-KCl eutectic using focused ion beam tomography. J. Nucl. Mater. *480*, 355–361. https://doi.org/10.1016/j.jnucmat.2016.07.036.

32. Withers, P.J., Bouman, C., Carmignato, S., Cnudde, V., Grimaldi, D., Hagen, C.K., Maire, E., Manley, M., du Plessis, A., and Stock, S.R. (2021). X-ray computed tomography. Nat. Rev. Methods Prim. *1*, 1–21. https://doi.org/10.1038/s43586-021-00015-4.

33. Kim, G.-Y., Lee, C.H., Yoon, D., Jang, J., and Lee, S.-J. (2021). Electrochemical deposition of U and RE elements using the stirred liquid cadmium cathode in LiCl-KCl molten salts. Sci. Technol. Nucl. Install. *2021*, 5788732. https://doi.org/10.1155/2021/5788732.